Measuring the cosmic expansion rate using 21-cm velocity acoustic oscillations

Debanjan Sarkar[*] and Ely D. Kovetz[†]

Physics Department, Ben-Gurion University of the Negev, Beersheba 84105, Israel

The fluctuations in the dark matter-baryon relative velocity field are imprinted as acoustic oscillations in the 21-cm power spectrum during cosmic dawn (CD). These velocity acoustic oscillations (VAOs) keep the imprints of the comoving sound horizon scale. In a previous work by Muñoz, it has been demonstrated that these VAOs can be treated as standard rulers to measure the cosmic expansion rate at high redshifts by considering a variety of Lyman-Werner feedback strengths and foreground contamination scenarios. Here we extend that analysis by using a modified version of the public code 21cmFAST. We use this code to simulate the VAOs in 21-cm power spectrum and forecast the potential to constrain $H(z)$ with the HERA radio telescope, taking into account the effects of Lyman-α heating, Lyman-Werner feedback and foregrounds, the dependence on various astrophysical parameters, and the degeneracy with cosmological parameters. We find that $H(z)$ can be measured with HERA at $\sim$0.3–6% relative accuracy in the range $11 < z < 20$, under different astrophysical and foreground scenarios, with uncertainties in the Planck cosmological parameters setting a $\sim$0.08–0.2% relative-error floor in the measurement. This accuracy is on par with most low-redshift measurements and can be helpful in testing various cosmological scenarios motivated by the ongoing "Hubble tension."

I. INTRODUCTION

Measuring the cosmic expansion history is one of the key goals of modern cosmology. It started with the famous discovery of the expanding universe by Edwin Hubble about a century ago [1]. Only about two decades ago, we came to know about the accelerating expansion of our Universe [2,3]. Ever since this discovery, a large number of theories have been proposed to explain this [4–7]. The theories can be divided broadly into two classes: (i) theories that propose the existence of dark energy, which has a negative equation of state (w) and the cosmological constant (Λ) with $w = -1$ [8] being the simplest example of it, (ii) theories that propose a modification in Einstein's theory of gravitation. Currently, we do not know which class of theories is correct, and we need to probe the cosmic expansion history [which we also call as Hubble expansion and denote as $H(z)$] in order to pin down this.

We have measured the current expansion rate of the universe which is also known as the Hubble constant (H_0). Measurements of the cosmic microwave background (CMB) using the Planck Satellite provide an extremely precise value of $H_0 = 67.4 \pm 0.5$ km/s/Mpc [9]. On the other hand, the local universe measurements like *SH0ES*, etc., which use observations of Cepheids in the

nearby galaxies, estimate the value of $H_0 = 73.0 \pm 1.0$ km/s/Mpc [10–12]. These two measurements are in $\sim 5 - \sigma$ disagreement with each other, and this is coined as the Hubble tension. For the time being, it is unclear whether this tension is caused by some new physics beyond the standard cosmological model [13–33], or some systematic effects [34] in either or both of the measurements. We, therefore, need other independent observations of the expansion rate in the local universe to draw a more robust conclusion on the cause of the H_0 tension, as well as at the high redshifts to test the cosmological theories of expansion.

The cosmological 21-cm signal will be observed over a large redshift range, as discussed in Refs. [35–45]. Detection of the baryon acoustic oscillation (BAO) features in the 21-cm intensity mapping power spectrum will provide the measurement of the expansion rate at $z \lesssim 6$ [46–49]. BAOs that occur due to the interaction between the baryon and photon fluids before recombination, generate supersonic relative velocity between DM and baryons just after recombination. This supersonic velocity prevents the formation of structures inside the mini halos (having masses in the range 10^5–10^7 M$_\odot$) [50–52] that form early in hierarchical structure formation scenario [53–55]. This delays the onset of the cosmic dawn (CD) epoch and directly affects the evolution of the 21-cm signal [56–64]. The fluctuations in the DM-baryon relative velocity field are imprinted as oscillations (just like BAOs), called velocity-induced acoustic

[*]debanjan@post.bgu.ac.il
[†]kovetz@bgu.ac.il

oscillations (VAOs), in the 21-cm power spectrum at large scales. Reference [63] shows that these unique VAOs follow a simple analytic shape, which is set at the time of recombination. Reference [64] first proposed to use the VAOs in the 21-cm power spectrum as a standard ruler to measure the expansion rate at high redshifts. Reference [64] showed that the 21-cm power spectrum measurements from the Hydrogen Epoch of Reionization Array (HERA) interferometer [65] should be able to measure the Hubble expansion rate $H(z)$ at $z = 15$–20 to percent-level precision, depending on the strength of Lyman-Werner (LW) feedback process [66–68] and foreground contamination.

The analysis in Ref. [64] is done at two fixed redshifts, and for a single set of cosmological and astrophysical parameters. Note that the onset of the CD, as well as the amplitude of the 21-cm signal depends on the cosmological and astrophysical parameters. For fixed sensitivity of telescopes and foreground contamination scenario, the amplitude of the 21-cm signal (or of the VAO peaks) mainly decides the signal-to-noise (SNR) with which VAOs can be detected. The best SNR occurs at redshifts which is determined by the combination of the model parameters and the telescope sensitivity. Note that, the binning of the power spectrum is also important as we need certain number of bins to clearly make out the VAO features which is important for the $H(z)$ measurement, and the VAO features will get smoothed out if less number of bins are used. Therefore, considering observations with a fixed telescope, we need to explore the effects of the different choice of the model parameters on the measurement of $H(z)$. The measurement of $H(z)$ is further subject to the additional heating effects like the Lyman-α heating which raise the IGM temperature if the poorly-constrained x-ray heating is not extremely efficient. The Lyman-α heating is due to the resonant scattering between Lyman-α photons and the IGM atoms [69–73].[1] In Ref. [76], we showed that Lyman-α heating suppresses the 21-cm power spectrum amplitude and this will likely affect the detectability of the VAOs.

Although the cosmological parameters are well measured by the Planck mission [9], there are still small uncertainties in the measured parameters. We need to estimate the errors propagated into the $H(z)$ measurement due to the uncertainties in the cosmological parameters.

In this paper, we simulate the 21-cm signal and model the VAOs in the 21-cm power spectrum using analytical prescriptions. Considering observations with the HERA

radio telescope, we quantify the relative error with which the expansion rate $H(z)$ can be measured under the different heating, LW feedback and foreground contamination scenarios. For each simulation scenario, we contained our analysis only to EoH, which occurs at $z < z_{\min}$ (where $z_{\min}$ refers to the redshift where the global 21-cm signal $\langle T_{21} \rangle = \langle T_{21} \rangle_{\min}$ has its minimum value), and measure $H(z)$ at $z = z_{\text{half}}$ where the global signal is $\langle T_{21} \rangle = (1/2) \langle T_{21} \rangle_{\min}$ and the signal-to-noise for VAO measurement is expected to be the highest. We also quantify the errors in $H(z)$ measurement introduced by the uncertainties in cosmological parameters from Planck measurements. The paper is organized as follows.

In Sec. II, we discuss the 21-cm signal from different epochs, briefly review the modelling of the DM-baryon relative velocity effect in the 21-cm power spectrum, and outline the procedure to measure the expansion rate $H(z)$ from the VAOs. In Sec. III, we discuss our simulations and model parameters. In Sec. IV, we present the sensitivity calculation for HERA radio telescope. We present our main findings in Sec. V, and conclude in Sec. VI. Note that, throughout our analysis, we have assumed flat Λ-CDM cosmology and use the fiducial cosmological parameters as given in Table I.

II. FORMALISM

A. 21-cm signal from different epochs

The 21-cm brightness temperature is given by [37,38]

$$T_{21} = \frac{T_S - T_{\text{CMB}}}{1 + z} (1 - e^{-\tau_{21}}),\tag{1}$$

where T_S is the spin temperature, T_{CMB} is the temperature of the background radiation which is usually assumed to be CMB with $T_{\text{CMB}} = T_{\text{CMB}}(z) = 2.7255(1 + z)$ K, and τ_{21} is the 21-cm optical depth which can be calculated as

$$\tau_{21} = \frac{3h A_{10} c \lambda_{21}^2 n_{\text{H I}}}{32\pi k_B T_S (1 + z)(dv_r/dr)}.\tag{2}$$

Here, h is the *Planck* constant, A_{10} is the Einstein A-coefficient for the 21-cm emission, c is the speed of light, λ_{21} is the wavelength of the 21-cm radiation, $n_{\text{H I}}$ is the neutral hydrogen number density, k_B is Boltzmann constant, dv_r/dr is the gradient of the comoving velocity along the line of sight which is taken to be $H(z)/(1 + z)$ where $H(z)$ is the Hubble rate.

The spin temperature can be calculated as [74,76]

$$T_S = \frac{x_{\text{rad}} + x_\alpha + x_c}{x_{\text{rad}} T_{\text{rad}}^{-1} + x_c T_K^{-1} + x_\alpha T_{c,\text{eff}}^{-1}},\tag{3}$$

where,

---

[1]Note that, there is another possible heating mechanism, called CMB heating, which results from the energy transfer from the radio background (which is dominated by the CMB) into the IGM, mediated by the Lyman-α photons [74]. Some recent works debate the significance of this effect [75], and we do not include CMB heating in our current analysis. We note that, our conclusions are not very sensitive to this, as the Lyman-α heating alone accounts for most of the heating effect.

$$x_{\text{rad}} = \frac{1 - e^{-\tau_{21}}}{\tau_{21}}, \qquad (4)$$

x_α and x_c are Wouthuysen-Field coupling [77–79] and collisional [80] coupling coefficients respectively, and $T_{c,\text{eff}}$ is the effective color temperature [38] for the Lyman-α radiation.

The standard evolution history of the 21-cm line is as follows. During the dark ages [81], collision coupled the spin temperature with the gas, producing 21-cm absorption for $z \gtrsim 30$. Collision, however, became inefficient as the universe expanded and the gas cooled and diluted further. This resulted in nearly no absorption until the advent of CD epoch ($z \sim 30$ for all the curves in Fig. 1) [82–84]. In this epoch the first luminous sources were formed. These sources emitted ample ultraviolet (UV) photons, which coupled T_S to T_K through a process called the Wouthuysen-Field (WF) effect [77–79], by which Lyman-α photons resonantly scatter between hydrogen atoms, imprinting T_K onto the hyperfine populations of hydrogen. This again produces 21-cm absorption and we call this period the
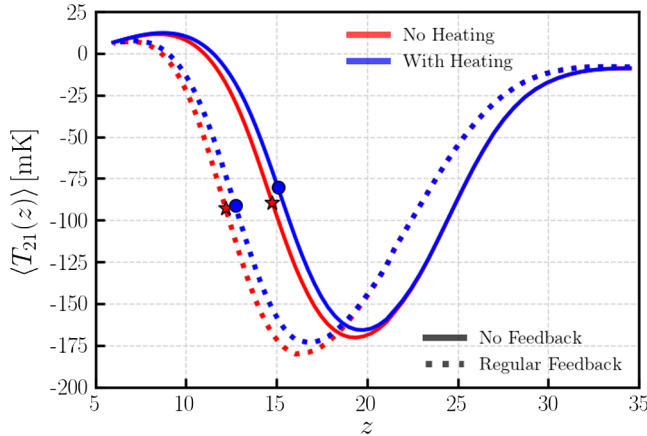

FIG. 1. This shows the global 21-cm signal $\langle T_{21} \rangle$ for our fiducial parameters and for two LW feedback scenarios. The solid curves show signal for no feedback, while the dashed curves show signal for regular feedback. The blue and red colors respectively indicate simulations with and without Lyman-α heating. Filled stars and filled circles represent the redshift values (which we denote by z_{half}, and the values are given in Table II) where $\langle T_{21} \rangle = (1/2)\langle T_{21} \rangle_{\text{min}}$. Here, $\langle T_{21} \rangle_{\text{min}}$ is the minimum value of the global signal which occurs at a redshift which we call z_{min}. The LW radiation feedback disturbs the star formation in the haloes, which delays the cosmic dawn epoch and all the epochs that follow. This can be seen clearly. Comparing solid and dashed curves, we see that all the different epochs like LCE, EoH (discussed in Sec. II A) are shifted toward the low redshifts by $\Delta z \sim 3$ when we introduce LW feedback. The Lyman-α heating heats up the IGM and, as a result, the EoH starts early for the models with Lyman-α heating. The blue curves show higher $\langle T_{21} \rangle_{\text{min}}$ than the red curves. Also the z_{min} and z_{half} values are slightly higher for the models with Lyman-α heating.

Lyman-α coupling era (LCE) (which ranges from $z \lesssim 30$ to $z \sim 20$ for the solid curves in Fig. 1). Later on, x-ray [72,85–87] and other photons, like Lyman-α [69,70], re-heat the IGM to temperatures $T_K \gtrsim T_{\text{CMB}}$, and switched the 21-cm signal to emission ($z < 12$ for the solid curves in Fig. 1). We call this period the epoch of heating (EoH) (For the solid curves in Fig. 1, it ranges from $z \lesssim 20$ to the beginning of reionization. The reionization for the curves considered began at $z \sim 10$ when the 21-cm global signal start to decline due to the lack of neutral hydrogen fraction in the IGM). Eventually at $z < 10$, i.e., at epoch of reionization (EoR) [88], high amount of UV photons ionized most of the neutral hydrogen that almost no 21-cm signal is left. Note that the minimum of the global signal, which is $\langle T_{21} \rangle_{\text{min}} \sim -165$ mK at $z \sim 19.5$ for the blue curve in Fig. 1, marks the end of LCE and beginning of EoH. The redshift, where this happens, we denote it by z_{min}.

The effect of relative velocities on the 21-cm brightness temperature during the LCE and EoH are different (see Ref. [63] for a comprehensive discussion on this). In LCE, the regions with large velocity produce shallower 21-cm absorption as the velocities impede star formation and thereby reduce Lyman-α photon production. Regions with small velocity produce deeper 21-cm absorption as the Lyman-α photon production is not hampered by much. This effect is most prominent at the redshift where $\langle T_{21} \rangle = (1/2)\langle T_{21} \rangle_{\text{min}}$ ($z \sim 25$ for the solid curves in Fig. 1) and we denote this redshift as $z_{\text{half}}^{\text{LCE}}$. This effect fades away gradually as we go toward the lower redshift where the Lyman-α coupling saturates. In EoH, the opposite happens. Patches with large velocities form fewer stars, thereby producing less heating, and therefore causing deeper 21-cm absorption. Patches with small velocities producing more heating, and therefore causing shallower 21-cm absorption. This effect also is most prominent at the redshift where $\langle T_{21} \rangle = (1/2)\langle T_{21} \rangle_{\text{min}}$ ($z \sim 15$ for the blue curve in Fig. 1) and we denote this redshift as $z_{\text{half}}^{\text{EoH}}$. This effect becomes less important as the IGM heating causes $T_S \gg T_{\text{CMB}}$ and the fluctuation due to T_S is negligible in Eq. (1). Due to the opposite nature at LCE and EoH, we have practically no effect of velocities at z_{min}. Reference [63] showed that the VAO amplitude in the 21-cm power spectrum is most prominent at $z_{\text{half}}^{\text{LCE}}$ and $z_{\text{half}}^{\text{EoH}}$, and the VAO amplitude is decreased as we move away from these redshifts. Based on the above discussion, we have no clear VAOs at z_{min}, as well as at redshifts where $T_S \gg T_{\text{CMB}}$ [89]. The VAOs also have higher amplitude during the EoH. Reference [63] also showed that the signal-to-noise for the VAO detection with the current generation of 21-cm experiments, like HERA, is higher during the EoH and expected to be maximum close to $z_{\text{half}}^{\text{EoH}}$. For this reason, from now onwards, we focus on EoH and we denote $z_{\text{half}} \equiv z_{\text{half}}^{\text{EoH}}$ for brevity.

B. Model the dark matter-baryon relative velocity effects in the 21-cm power spectrum

In this section, we discuss the modulation of the 21-cm power-spectrum due to the DM-baryon relative velocity. The 21-cm power-spectrum is defined as,

$$\Delta^2_{21}(k) = \frac{k^3 P_{21}(k)}{2\pi^2} [\text{mK}^2], \tag{5}$$

where $P_{21}(k) = \langle \tilde{T}_{21}(k)\tilde{T}^*_{21}(k)\rangle$ and $\tilde{T}_{21}(k)$ is the Fourier transform of $T_{21} - \langle T_{21}\rangle$. The modulation of the 21-cm power spectrum due to the dark-matter baryon relative velocities can be apprehended from the statistics of the collapsed baryonic density. The effect of bulk relative velocities is very similar to that of the baryonic pressure, which suppresses the accumulation of baryons in the haloes. As the gas accreted into the DM halo, the relative velocity increases the effective sound speed. This further increases the critical mass scale of a halo that can retain the baryons and decreases the baryon collapsed fraction [57,60,61,90–96]. The effect of the relative velocities on the amplitude of the 21-cm brightness temperature power spectrum can be parametrized as [63]

$$\Delta^2_{21,\text{vel}}(k, z) = A_{\text{vel}}(z)\Delta^2_{v^2}(k, z)|W(k, z)|^2, \tag{6}$$

where A_{vel} is some redshift-dependent amplitude of fluctuations. The window function $W(k, z)$ depends on the different contributors to the 21-cm power spectrum such as the coupling to the Lyman-α photons and x-ray heating. Here, $\Delta^2_{v^2}(k)$ as the power spectrum of the quantity

$$\delta_{v^2} = \sqrt{\frac{3}{2}}\left(\frac{v^2_{\text{cb}}}{v^2_{\text{rms}}} - 1\right), \tag{7}$$

which accurately captures the shape of the effect of relative velocities on the observables for the scales of interest and the "streaming" bulk relative velocity (v_{cb}) can be approximated with a root-mean-squared value $v_{\text{rms}} \simeq 30 \text{ km s}^{-1}$ at recombination [58]. Note that, A_{vel} is a model-dependent amplitude that is not directly observable. The VAOs are statistically independent from the density fluctuations at first order. Therefore, the amplitude of the 21-cm power spectrum can be written as [63]

$$\Delta^2_{21}(k, z) = \Delta^2_{21,\text{vel}}(k, z) + \Delta^2_{21,\text{nw}}(k, z), \tag{8}$$

where $\Delta^2_{21,\text{nw}}(k, z)$ is the component of the 21-cm power spectrum *without* VAOs. Following Ref. [63], we parametrize the $\Delta^2_{21,\text{nw}}(k, z)$ as a smooth polynomial,

$$\ln[\Delta^2_{21,\text{nw}}(k, z)] = \sum_{i=0}^{n} c_i(z)[\ln k]^i, \tag{9}$$

where $c_i(z)$ are coefficients we fit for using simulations as discussed in Ref. [63]. We model the velocity power spectrum as in Ref. [64] using the form we defined in Eq. (6). We calculate the window function and the amplitude $A_{\text{vel}}(z)$ for a given model using 21cmvFAST [63] (which we shall discuss later), and calculate $\Delta^2_{v^2}$ for a given cosmology. We calculate the transfer function of the relative velocities at the end of recombination using CLASS Boltzmann code [97–100], which is then used as an initial condition for our simulations.

C. Measurements of $H(z)$ from acoustic peaks

Since VAOs are sourced by BAOs, they keep the imprints of the comoving sound horizon scale $r_d \approx 150$ Mpc at the baryon drag era ($z_d \approx 1060$). The separation of the VAO peaks in the Fourier-space, $\Delta k = 2\pi/r_d$, gives the estimate of r_d and the VAO features in the CD 21-cm power spectrum preserves this well-known distance scale [64]. This r_d can be used as a standard ruler, and together with the Alcock-Paczyński (AP) [101–105] test on the power spectrum data, we can recover the expansion rate $H(z)$. According to AP effect, the parallel $k_\parallel$ and perpendicular $\mathbf{k}_\perp$ wave vectors (defined with respect to the line-of-sight direction) get shifted to values $k_\parallel/a_\parallel$ and $\mathbf{k}_\perp/a_\perp$ when assuming wrong fiducial cosmology [104]. Here $a_\parallel = (H^{\text{fid}}(z)r_d^{\text{fid}})/(H(z)r_d)$ and $a_\perp = (D_A(z)r_d^{\text{fid}})/(D_A^{\text{fid}}(z)r_d)$ are two AP parameters, where $H(z)$ is the Hubble expansion rate, $D_A(z)$ is the angular diameter distance, and superscript "fid" denotes their fiducial values. Therefore, measuring the shift in the VAO peaks, we can constrain $a_\parallel$ and $a_\perp$, and thereby measure $H(z)$ and $D_A(z)$ [64].

III. SIMULATION

We use a modified version of the publicly available 21cmvFAST[2] [63] semi-numerical code to generate the observable 21-cm signal. 21cmvFAST mainly includes the effects of DM-baryon relative velocity and LW radiation feedback into the 21-cm calculations, using precalculated input tables of quantities that depend on these effects, given for a single set of cosmological parameters (matching Planck cosmology). Note that, 21cmvFAST itself is a modification of the public code 21cmFAST[3] [106], widely used to simulate the 21-cm signal. We modify 21cmvFAST in order to interface it with CLASS [97–100], which enables it to calculate all required quantities on the fly for any cosmological scenario and any set of input cosmological parameters. We have also introduced the

---

[2]github.com/JulianBMunoz/21-cmvFAST.
[3]github.com/21cmfast/21cmFAST.git.

CMB and Lyman-α heating effects in the code. The details about these implementations can be found in Ref. [76].

The 21cmvFAST [63] code requires a number astrophysical and cosmological parameters as input. The astrophysical parameters are: ζ (describes the efficiency of ionizing photon production), λ_{MFP} (mean free path of the ionizing photon), $V_{\mathrm{cool}}^{(0)}$ (minimum halo mass for molecular cooling in the absence of relative velocity), $V_{\mathrm{cool}}^{\mathrm{HI}}$ (minimum halo mass for atomic cooling), $\log_{10}(L_{\mathrm{X}}/\mathrm{SFR})$ (log of x-ray luminosity, normalized by the star formation rate SFR, in units of $\mathrm{erg\,s^{-1}}M_{\odot}^{-1}\,\mathrm{yr}$), α_X (x-ray spectral index), $f_{\star}^0$ (fraction of baryons in stars), E_{min} (threshold energy, below which we assume all x-rays are self-absorbed near the sources).

We assume a flat universe with the following cosmological parameters: h (Hubble parameter), $\sigma_{8,0}$ (standard deviation of the current matter fluctuation smoothed at scale $8\,h^{-1}$ Mpc) $\Omega_{\mathrm{m}0}$ (total matter density at present), $\Omega_{\mathrm{b}0}$ (total baryon density at present), n_s (spectral index of the primordial power spectrum), T_{CMB} (current CMB temperature). The fiducial values of these parameters are given in Table I.

We run our modified version of 21cmvFAST with box sizes 600 Mpc and 1 Mpc resolution to compute the 21-cm global signal and fluctuations. We verified that the choice of a 600 Mpc box retains sufficient v_{cb} power at large scales and the power spectra show good convergence with a 900 Mpc box results. For a better visualization of the VAO shape, we increase the number of bins while calculating the 21-cm power spectrum. This, however, decreases the number of **k**-modes and increases the Poisson noise in each bin.

Reference [63] has parametrized the effect of LW radiation feedback on the minimum halo mass M_{cool} that can form stars as,

TABLE I. Our main simulation parameters and their fiducial values.

Parameters	Fiducial values
ζ	20
λ_{MFP}	15 Mpc
$V_{\mathrm{cool}}^{(0)}\,[\mathrm{km/s}]$	4
$V_{\mathrm{cool}}^{\mathrm{HI}}\,[\mathrm{km/s}]$	17
$\log_{10}(L_{\mathrm{X}}/\mathrm{SFR})$	39
α_X	1.2
$f_{\star}^0$	0.05
E_{min}	0.2 keV
$\sigma_{8,0}$	0.8102
h	0.6766
$\Omega_{\mathrm{m}0}$	0.3111
$\Omega_{\mathrm{b}0}$	0.0489
n_s	0.9665
T_{CMB}	2.7255

$$M_{\mathrm{cool}}(z, F_{\mathrm{LW}}) = M_{\mathrm{cool}}(z, 0) \times [1 + B(F_{\mathrm{LW}})^{\beta}], \qquad (10)$$

where $M_{\mathrm{cool}}(z, 0)$ is the minimum halo mass without the effect of LW feedback, F_{LW} is the LW radiation flux, and the parameters β and B defines the strength of the feedback. We have considered three LW radiation feedback strengths[4] in our simulations (i) no feedback ($B = 0$), (ii) low feedback ($B = 4$, $\beta = 0.47$) and (iii) regular feedback ($B = 7$, $\beta = 0.47$), as defined in Ref. [63]. Further, we only consider Lyman-α heating in our analysis due to the uncertainties in the CMB heating efficiency as discussed in Sec. I. For weak x-ray efficiency, Ref. [76] showed that Lyman-α heating dominates most of the EoH, and our results largely do not depend on the CMB heating. In our fiducial simulations, we consider $\log_{10}(L_{\mathrm{X}}/\mathrm{SFR}) = 39$. Recently, Ref. [108] showed that the HERA Phase-I data [109] suggests high x-ray efficiency ($\log_{10}(L_{\mathrm{X}}/\mathrm{SFR}) > 40$) for high redshift galaxies. However, the analysis in Ref. [108] does not incorporate Lyman-α heating, which will presumably bring down the preferred $\log_{10}(L_{\mathrm{X}}/\mathrm{SFR})$ value. Based on this, we set $\log_{10}(L_{\mathrm{X}}/\mathrm{SFR}) = 39$ to compensate for the extra heating caused by Lyman-α photons. Note that, for high x-ray efficiency, the Lyman-α heating is subdominant [76].

As defined earlier, $\Delta_{21,\mathrm{nw}}^2(k, z)$ is the power spectrum of the 21-cm signal without the VAOs. VAOs result from the fluctuations in the v_{cb} field. To suppress the fluctuations in the v_{cb} field, we replace the v_{cb} values with $v_{\mathrm{cb}} = \langle v_{\mathrm{cb}} \rangle = 0.92 v_{\mathrm{rms}}$ in the simulations, as suggested in Ref. [63]. This choice only suppresses the VAOs in the 21-cm power spectrum, without altering the global signal.

IV. SENSITIVITY CALCULATION FOR HERA

The measurement of $H(z)$ depends on the detectability of the of the VAO peaks and their shift. The detectability, however, depends on the sensitivity of the radio telescope and the foreground contamination. In the 21-cm observations, the foreground is several order of magnitude brighter than the signal and expected to contaminate a significant amount of Fourier space [110–113]. In the $k_{\perp} - k_{\parallel}$ space,

---

[4]Note that, Ref. [64] has considered low, regular and high feedback scenarios in their analysis, with regular feedback being their fiducial. In the high feedback scenario $B = 7$, $\beta = 0.47$, and the effect of LW photons and the relative velocities is assumed to be fully uncorrelated which increases M_{cool} substantially compared to the regular feedback scenario. We have not considered the high feedback scenario in our analysis for the following reason. Recently, Ref. [107] has simulated the effects of the LW feedback using $B = 2$, $\beta = 0.6$. They stated that the most recent simulations suggest that B and β values lie in the ranges of $\{0.8, 3\}$ and $\{0.5, 0.9\}$, respectively, with $B = 3$ representing very strong feedback. Given this, the value of $B = 7$ in the regular feedback scenario is already very high. Therefore, we restrict the maximum feedback strength in our analysis to the regular feedback scenario. We included the no feedback scenario for comparison, and the low feedback scenario is the fiducial case in our analysis.

TABLE II. This shows the projected $1 - \sigma$ relative errors on $H(z)r_d$ for our fiducial parameter set (Table I), under the different feedback, heating and foreground assumptions. We also mention the z_{half} values for each simulation. We have considered 540 days of HERA observation in all cases.

Model	Feedback	z_{half}	$\Delta(Hr_d)/(Hr_d)\%$		
			Optimistic	Moderate	Pessimistic
No Ly-α Heating	No	14.8	0.3	0.62	1.82
	Low	12.7	0.51	1.14	3.51
	Regular	12.2	0.73	1.51	4.62
With Ly-α Heating	No	15.1	0.44	0.86	2.64
	Low	13.3	0.63	1.31	3.94
	Regular	12.7	0.9	1.84	5.53

where $k_\parallel$ and $k_\perp$ are the components of the wave vector respectively parallel and perpendicular to the line-of-sight direction, the contaminated part of the Fourier space looks like a "wedge" [114,115]. Following Refs. [115,116] the extent of the foreground wedge can be parametrized by assuming that all wave numbers with $k_\parallel$ below

$$k_\parallel^{min} = a + b(z)k_\perp \qquad (11)$$

are contaminated, where $b(z)$ accounts for the chromaticity of the antennae, and a is a constant superhorizon buffer. Given the uncertainty in foreground contamination, we consider three cases [64]. In the "optimistic" case, where we assume minimum amount of foreground contamination, we set $a = 0$ and $b(z)$ is determined by the primary beam. In the "moderate" and "pessimistic" foreground contamination scenarios, we assume $b(z)$ is determined by the horizon limit, and consider $a = (0.05, 0.1) h$ Mpc^{-1} respectively. Further more, the baselines are coherently added in case of optimistic and moderate foregrounds, while only the instantaneously redundant baselines are combined coherently in the pessimistic case.

For the forecast, we consider the HERA 21-cm intensity mapping experiment [65]. HERA is located in the Karoo Desert of South Africa and is designed to measure the 21-cm fluctuations from CD (50 MHz or $z \sim 27$) to the reionization era (225 MHz or $z \sim 5$). The final stage of HERA is expected to have 350 antenna dishes, each with a diameter of 14 m. Out of the 350 dishes, 320 will be placed in a close-packed hexagonal configuration and the remaining 30 will be placed at longer baselines. We calculate the sensitivity of HERA using the publicly available package 21cmSense[5] [115,116]. This code accounts for the $u - v$ sensitivities of each antenna in the array, and calculates the possible errors in the 21-cm power spectrum measurement, including cosmic variance. For details, the reader is referred to Ref. [76]. We consider a total of 540 days of observation per redshift with 6 hours of observation per day. Following

Ref. [64], we bin the k-modes logarithmically in order to resolve the VAO peaks more clearly.

V. RESULTS

A. Effect of Lyman-α heating

In this section, we discuss the effects of Lyman-α heating on the 21-cm global signal and power spectrum. Figure 1 shows the 21-cm global signal for our fiducial model parameters (see Table I) and for two different LW feedback scenarios: no feedback and regular feedback. We find that the cosmic dawn and the subsequent epochs are delayed (by $\Delta z \sim 3$) for the regular feedback cases, compared to the no feedback cases. As a result, $\langle T_{21} \rangle_{min}$ occurs at lower z_{min} (making z_{half} lower as well) for the models with regular feedback. Also, $\langle T_{21} \rangle_{min}$ values are more negative for the models with regular feedback. Now considering a particular feedback case, we see that $\langle T_{21} \rangle_{min}$ value is raised by a little and occurs at a slightly higher z_{min} when we introduce the Lyman-α heating. In the Lyman-α heating scenario, the Lyman-α photons heat the IGM and raise the kinetic temperature T_K. As a result, contrast between T_{CMB} and T_S is decreased and this increases $\langle T_{21} \rangle_{min}$. The z_{half} values are also slightly higher for the models with Lyman-α heating, compared to no heating. The z_{half} values for different LW feedback strengths and Lyman-α heating scenarios are given in Table II. Note that, the Lyman-α heating is more efficient for the models with low x-ray efficiency. In our fiducial models with $\log_{10}(L_X/SFR) = 39$, we have sufficient contribution from the Lyman-α heating. We find that for models with $\log_{10}(L_X/SFR) > 40$, the Lyman-α heating contribution is negligible. Overall, Lyman-α heating tries to decrease the contrast between T_{CMB} and T_S and this has a significant effect on the 21-cm power spectrum, which we shall see next.

Figure 2 shows the 21-cm power spectrum $\Delta_{21}^2(k)$ at $z = z_{half}$ (see Table II) for the same simulations shown in Fig. 1. We see that both feedback and Lyman-α heating decrease the amplitude of the 21-cm power spectrum and VAO peaks. The difference $\Delta z_{half} \sim 3$ between regular and no feedback cases is large, and we cannot directly compare the feedback effects as they occur at very different redshifts.
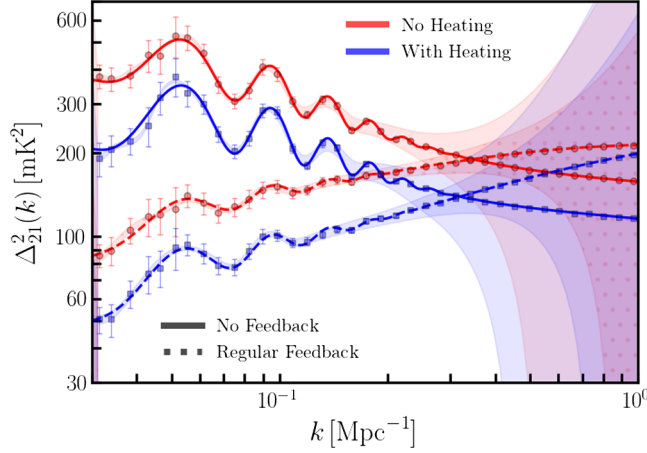

FIG. 2. This shows the 21-cm power spectrum $\Delta_{21}^2(k)$ as function of wave vector k at redshifts z_{half} where the global signal is $\langle T_{21} \rangle = (1/2)\langle T_{21} \rangle_{\text{min}}$ (shown using filled stars and circles in Fig. 1). Here we show the same simulations as in Fig. 1 and all the different lines and colors carry the same meaning. Here the simulated data are shown with points and the error bars show the 1-σ Poisson error at each bin. The shaded regions show errors obtained for HERA using 21cmSense under the optimistic foreground assumption. The solid and dashed lines represent the fits of the model given in Eq. (8). We see that feedback reduces the amplitude of the power spectrum and the associated VAO peaks. LW feedback disturbs the star formation in the smaller haloes and decreases the fluctuations in the 21-cm field introduced by the relative velocity. Although the z_{half} values are smaller for the regular feedback cases, compared to no feedback cases, the suppression is significant. Similarly, Lyman-α heating also decreases the amplitude of the 21-cm power spectrum and VAOs. The Lyman-α heating increases the IGM temperature, and thereby decreasing the contrast between T_{CMB} and T_{S}.

However, previous studies (like Ref. [76]) showed that for a fixed z, LW feedback suppresses the amplitude of the power spectrum significantly. On the other hand, the difference $\Delta z_{\text{half}} \sim 0.3$–$0.5$ between with and without Lyman-α heating scenarios is small, and we can directly compare the heating effects here. We see that Lyman-α heating suppresses the VAO peaks by a factor of ~ 2. Not only that, it pushes z_{half} at a higher value. Both of these effects, influence the effective signal-to-noise [63] with which VAO peaks can be detected, and affect the measurement of $H(z)$, which we shall see later.

B. Relative error on $H(z)r_d$ measurement

In this section, we discuss the relative error on the measurement of $H(z)$ based on the method outlined in Sec. II C. We generate the mock data, which is the 21-cm power spectrum $\Delta_{21,\text{data}}^2$, using the 21cmvFAST simulation (discussed in Sec. III). For the first part of our analysis, we generate data using our fiducial model parameters (Table I) for three different LW feedback strengths and Lyman-α heating (as given in Table II). We define our likelihood $\mathcal{L}$ at each redshift as

$$-\log \mathcal{L} = \frac{1}{2} \sum_{k-\text{bins}} \frac{[\Delta_{21,\text{data}}^2(k) - \Delta_{21,\text{model}}^2(k, \mathbf{p})]^2}{\text{var}[\Delta_{21}^2(k)]}, \quad (12)$$

where $\Delta_{21,\text{model}}^2$ is the model power spectrum defined in Eq. (8), $\text{var}[\Delta_{21}^2(k)]$ is the expected variance of the 21-cm power spectrum measurement for HERA which we generate using the 21cmSense package for three different foreground scenarios as discussed in Sec. IV. The sum here is over the k-bins, $\mathbf{p}$ is the parameter vector which we shall specify later. The small k-bins are mostly dominated by cosmic variance and foregrounds, and the large k-bins are dominated by the telescope noise (see Fig. 2). The large k-modes also do not show VAOs. Based on these, we restrict the k-range to $\{0.03, 0.5\}$ Mpc^{-1} for our analysis. We sample the likelihood space with the PYTHON package EMCEE[6] [117].

As discussed in Ref. [64], the current generation 21-cm observations will mostly measure the modes with $k_\parallel \gg k_\perp$ due to the shape of the foreground wedge. As a consequence, 21-cm observations will not measure the AP parameter $a_\perp$ very precisely. Following Ref. [64], we keep $a_\perp$ fixed during in our fitting and vary $a_\parallel$ in our MCMC analysis. However, we have checked that the inclusion of $a_\perp$ in the MCMC analysis does not affect our final results and we discuss this point in Sec. VI.

We define our data vector $\mathbf{p} = \{a_\parallel, A_{\text{vel}}, c_i\}$, where c_i are the coefficients of the model for the smooth part of the 21-cm power spectrum $\Delta_{21,\text{nw}}^2(k, z)$ [Eq. (9)], and A_{vel} is the amplitude of the VAOs [Eq. (6)]. We impose the following priors on the parameters: $0.8 \leq a_\parallel \leq 1.2$, $0 \leq A_{\text{vel}} \leq 10^3$ mK^2, $-20 \leq c_i \leq 20$. These priors are broad enough to fit the 21-cm power spectrum for all of the different simulations considered here. We find that $n = 2$ in Eq. (9) is sufficient to model the smooth part of the 21-cm power spectrum for our k range of fitting, and we include coefficients $\{c_0, c_1, c_2\}$ in our analysis. Note that the parameters $(A_{\text{vel}}, c_0, c_1, c_2)$ depend mostly on the astrophysics. Therefore, marginalization over these parameters would mean marginalizing over the astrophysical parameters.

In Sec. II A, we discussed that the SNR for VAO measurement is expected to be maximum at z_{half} (defined for EoH). We restrict our analysis only to z_{half} which is different for the different simulations considered here (see Table II). We run the MCMC analysis, based on the likelihood in Eq. (12) and the prior range discussed above, and present the $1 - \sigma$ marginalized relative error on Hr_d (obtained from the fitting of $a_\parallel$) in Table II. We first consider the models without the Lyman-α heating. For no LW feedback, $z_{\text{half}} = 14.8$ and we find that it is possible to measure Hr_d with 0.3%, 0.62%, 1.82% accuracy for optimistic, moderate and pessimistic foreground contamination respectively. When we consider low and regular

---

[6]github.com/dfm/emcee.

feedback, z_{half} is shifted at lower value. Note that, the sensitivity of HERA is increased when we go to the low redshifts, and we expect to have better measurement of Hr_d at low redshifts. However, as mentioned earlier, the measurement of Hr_d (or VAOs) also depends on the amplitude of the VAOs. LW feedback of any form disturbs star formation in small haloes, which not only delay the cosmic dawn, but also dampens the VAO features. We actually see this in Table II. For low ($z_{half} = 12.7$) and regular ($z_{half} = 12.2$) feedback scenarios, it is possible to measure Hr_d with $(0.51, 1.14, 3.51)\%$ and $(0.73, 1.51, 4.62)\%$ relative accuracy for the (optimistic, moderate, pessimistic) foregrounds. Now considering models with Lyman-α heating, we overall see that z_{half} is higher and the constraints in each case are ~ 1.5 times worse in comparison to models without Lyman-α heating. We have already discussed in the previous section that Lyman-α heating starts EoH earlier and make z_{half} higher where the sensitivity of HERA decreases. Not only that, Lyman-α heating also decreases the amplitude of the 21-cm power spectrum, as well as of the VAOs. These two effects decreases the detectability of VAOs and thereby increase the relative error on the Hr_d measurement.

Note that, Ref. [64] has performed the analysis at two redshifts $z = 16$ and 18 for different simulations. Their analysis helped to compare the measurements of Hr_d at each z for different simulation scenarios. However, our aim here is different. The astrophysics is largely unknown at high redshifts and z_{half} depends very much on the model of astrophysics (as well as cosmology). We want to quantify the best possible measurement of Hr_d (which occurs close to z_{half}) for all the different astrophysical and cosmological scenarios. To do so, we run 108 different simulations by changing the model parameters around the fiducial set (which ultimately change z_{half}), and perform the fitting process discussed above to determine

the 1-σ relative error on Hr_d at z_{half}. We have changed the following parameters and we mention the range, over which the parameters are changed, in the curly brackets. The parameters are: $\zeta = \{18, 22\}$, $\lambda_{MFP} = \{10, 20\}$ Mpc, $V_{cool}^{(0)} = \{3.5, 4.5\}$ km/s, $\log_{10}(L_X/SFR) = \{38, 41\}$, $\alpha_X = \{1.0, 1.5\}$, $f_\star^0 = \{0.02, 0.15\}$, $E_{min} = \{0.1, 0.5\}$ keV, $\Omega_{m0} = \{0.2911, 0.3311\}$, and $\Omega_{b0} = \{0.0459, 0.0519\}$. For each parameter, we have considered four different values in the given range. Note that for each set of parameters, we have considered three LW feedback strengths. We also include Lyman-α heating in all the simulations. For comparison, we plot the 21-cm global signals and power spectra for all the simulations in Figs. 3 and 4 respectively. Instead of denoting each simulation with their corresponding parameter sets, we denote them with their corresponding $\langle T_{21} \rangle_{min}$ and z_{min} values (which are different for the different set of parameters) and present the fitting results in Fig. 5. We also plot the corresponding z_{half} values for each simulation in Fig. 6. We discuss our fitting results in the following paragraph.

From Fig. 5, we see that the z_{min} and $\langle T_{21} \rangle_{min}$ values are positively correlated for the range of parameters that we have chosen. Considering Fig. 3, we find that models e.g., with low LW feedback, high x-ray heating, large $f_\star^0$, large Ω_{m0}, start the EoH early and we see higher $\langle T_{21} \rangle_{min}$ and z_{min} values for these models. The corresponding z_{half} values also increase for these models (with respect to the fiducial model) as can be seen from Fig. 6. Considering the overall results from Fig. 5, we find that for $z_{min} < 22$ ($z_{half} < 16$) and $\langle T_{21} \rangle_{min} < -100$ mK, measurement of Hr_d is possible with $\lesssim 1.5\%$, $\lesssim 3\%$ and $\lesssim 6\%$ accuracy for optimistic, moderate and pessimistic foreground scenarios. At $z_{min} > 22$, we see that the errors somewhat increase and we find that most models have high x-ray heating in this range. We also see that for a fixed LW feedback strength, the errors mostly decrease as we go to smaller z_{min} (or z_{half}).
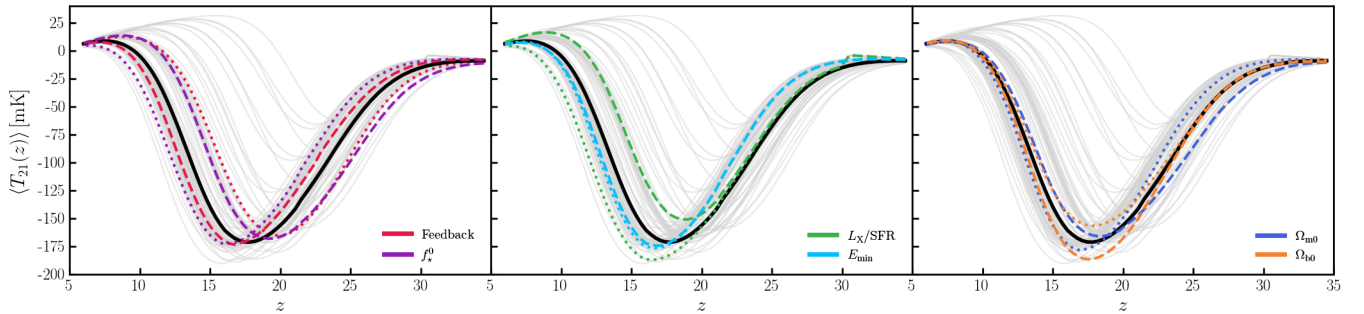

FIG. 3. This shows the 21-cm global signals for different set of model parameters. We change the various model parameters around the fiducial set (given in Table I) and generate global signals for 108 simulations. We show the fiducial signal, which is for the fiducial parameters and low LW feedback, in thick solid-black line and the rest of the global signals are plotted in thin solid-gray lines. To show the dependence of the signal on a few parameters, we highlight some of the global signals in colors. The parameters and the associated colors are given in the legend. The signals for parameter values above and below the fiducial are show respectively with dashed and dotted lines. The parameters along with their values above and below the fiducial are as follows: Feedback = {Regular, No}, $\log_{10}(L_X/SFR) = \{38.5, 39.5\}$, $f_\star^0 = \{0.02, 0.15\}$, $E_{min} = \{0.5, 0.1\}$ keV, $\Omega_{m0} = \{0.3311, 0.2911\}$, and $\Omega_{b0} = \{0.0519, 0.0459\}$. Note that, for all the simulations we have considered Lyman-α heating.
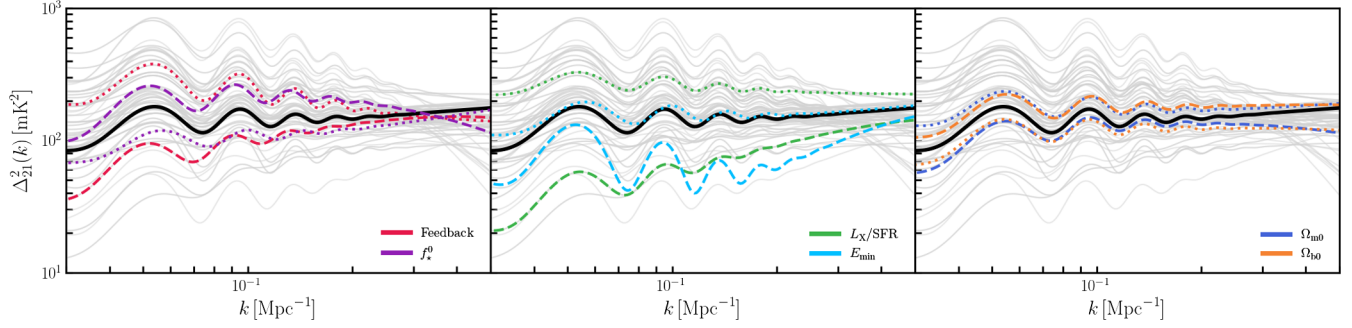
FIG. 4.   This shows the 21-cm power spectra at $z = z_{half}$ for the same simulations shown in Fig. 3. Different colors and line types carry the same meaning as in Fig. 3. Note that for all the simulations, we have plotted the best fit 21-cm power spectra [given by the model in Eq. (8)] under the optimistic foreground assumption.
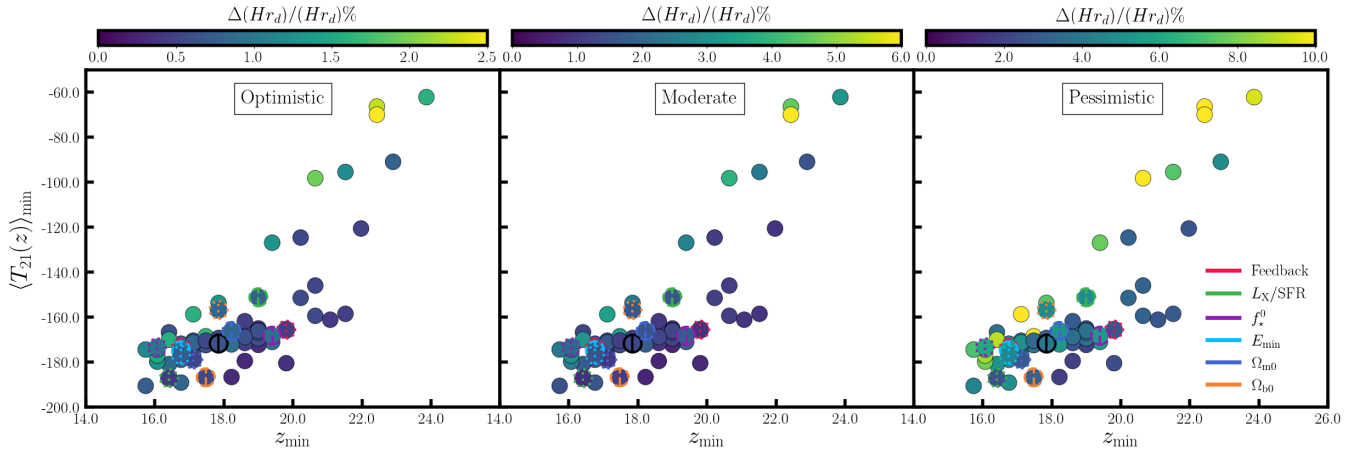

FIG. 5.   This shows the projected $1 - \sigma$ relative errors on $H(z)r_d$ (obtained from the fitting of $a_{\parallel}$ as discussed in Sec. V B) for various simulations mentioned in Figs. 3 and 4. Each simulation here is denoted by its corresponding $(z_{min}, \langle T_{21} \rangle_{min})$ values, which we show as circles, while the color on the circles show the $1 - \sigma$ relative errors on Hr_d. We have shown results for three foreground removal scenarios: optimistic, moderate and pessimistic. The circles corresponding to the highlighted parameters in Figs. 3 and 4 are shown here with colored edges and central bars. The different colors of the edges and the bars represent the parameters (given in the legend), while the dashed and dotted line styles respectively represent values above and below the fiducial.
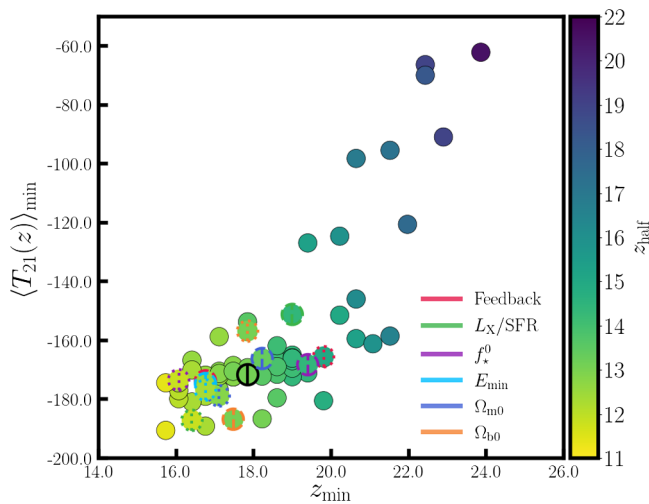

FIG. 6.   For the same circles shown in Fig. 5, different colors here show the z_{half} values for the simulations denoted by their $(z_{min}, \langle T_{21} \rangle_{min})$ values.

As discussed previously, sensitivity of HERA is increased as we go to lower redshifts and this helps to reduce the errors in the measurement of Hr_d. The error also depends on other factors, which we shall discuss below.

We now discuss the effects of the parameters, highlighted with colors in Fig. 5, in the measurement of Hr_d. Note that, the effects will be discussed with respect to the fiducial parameter set. Also, we shall take help from Figs. 3 and 4 at each step in order to explain and interpret the results plotted in Fig. 5. We have already discussed the effects of the LW feedback, increasing which delays the EoH (See Fig. 3), the VAOs tend to get erased (See Fig. 4) and ultimately the errors in Hr_d are increased (Table II). Considering the x-ray heating parameter $\log_{10}(L_X/SFR)$, we find that EoH occurs early (Fig. 3) and z_{min} (or z_{half}) is higher when we increase $\log_{10}(L_X/SFR)$ with respect to the fiducial value and vice versa. Higher x-ray heating also damps the VAO amplitude as can be seen from Fig. 4. If we combine both effects, we see that the measurement errors

increase and decrease when $\log_{10}(L_X/\text{SFR})$ is respectively increased and decreased. Next we discuss the effects of $f_\star^0$ which controls the fraction of baryons into stars. Increasing and decreasing $f_\star^0$ from the fiducial value make $z_{\min}$ (or z_{half}) respectively higher and lower (Fig. 3). Not only that, the VAO amplitude is also higher for the models with high $f_\star^0$ and vice versa (Fig. 4). These two competing effects decide the measurement errors of Hr_d. For the values $f_\star^0 = 0.02$ and 0.15, which we have highlighted in Fig. 5, we find that the error is slightly lower for the model with $f_\star^0 = 0.15$, although z_{half} is considerably higher for this model. This again shows the importance of the VAO amplitude to decide the signal-to-noise in Hr_d measurement. Next we consider $E_{\min}$. We see that higher $E_{\min}$ increases $z_{\min}$ (or z_{half}) (Fig. 3) and damps the VAOs at large k (Fig. 4). Opposite happens for lower $E_{\min}$. As a result, measurement errors of Hr_d increases for high $E_{\min}$ models and vice versa (Fig. 5). Considering Ω_{m0}, we find that CD and subsequent epochs start early for models with high Ω_{m0}, which also increases $z_{\min}$ (or z_{half}) (Fig. 3). However, high Ω_{m0} dampens the VAO features, and VAOs are more pronounced for models with low Ω_{m0} (Fig. 4). Combination of these two effects make Hr_d measurement error high for models with high Ω_{m0}, and the opposite is also true. The effect of Ω_{b0} is not straightforward to guess. Naively once expects that $z_{\min}$ will be higher for models with high Ω_{b0}, as the CD and EoH are expected to start early for these models. However, we find that, T_K is lower for the models with high Ω_{b0}. Also the coupling between T_S and T_K is higher for these models. As a result, we find that both $z_{\min}$ (also z_{half}) and $\langle T_{21}\rangle_{\min}$ are slightly lower for the model with high Ω_{b0} (Fig. 3). Also, high Ω_{b0} boosts VAO amplitude (Fig. 4). All these effects together help in reducing the error in Hr_d for models with high Ω_{b0}. Overall, we can conclude that, the measurement errors of Hr_d are smaller for models that produce lower $z_{\min}$ (or z_{half}) and $\langle T_{21}\rangle_{\min}$, without damping the VAOs considerably.

C. Errors due to the uncertainties in cosmological parameters

The cosmological parameters are very precisely constrained by the Planck measurements [9]. For this reason, we often do not consider the uncertainties in the cosmological parameters, when we study the 21-cm signal. We assume that most of the uncertainties are introduced by the astrophysical parameters. However, we have already seen that for optimistic foreground contamination, measurement of Hr_d is possible with subpercent precision. In this scenario, we must check how much does the uncertainty in cosmological parameters influence the measurement of Hr_d (or $a_\parallel$). However, it is not straight forward to infer this. Here, we follow the technique introduced in Ref. [118] to determine this uncertainty. $a_\parallel(\mathbf{p})$ is a function of cosmological parameters and we denote the parameter vector by

$\mathbf{p}$, where $\bar{\mathbf{p}}$ represents its fiducial value. The fiducial values are given in Table I. We now consider a small variation around the fiducial parameter values $\bar{p}_m$ and assume the following linearized relation

$$\left(\frac{\Delta a_\parallel}{a_\parallel}\right)(\bar{\mathbf{p}}) = \sum_m \left(\frac{\partial \ln a_\parallel}{\partial p_m}\right)\Delta p_m, \qquad (13)$$

where the index m denotes the different cosmological parameters, and the coefficients $\frac{\partial \ln a_\parallel}{\partial p_m}(\bar{\mathbf{p}})$ capture the variation in $(\Delta a_\parallel/a_\parallel)$ due to the variation Δp_m in any cosmological parameters. We calculate these coefficients from simulations. We consider the 21-cm power spectra at $z = z_{\text{half}}$ for each set of simulations discussed in Table II. We then perform the fitting process discussed in Sec. V B to determine the parameters $\{a_\parallel, A_{\text{vel}}, c_0, c_1, c_2\}$ for the same range $k \in \{0.03, 0.5\}$ Mpc^{-1} as used in Sec. V B. We have considered only the Poisson errors at each k-bin (shown in Fig. 2) during the fitting, and ensure that we get best fit $a_\parallel \approx 1$ which is what we expect to get for a correct set of cosmology. In this fitting process, we also checked that the errors on the best fit parameters are small enough that they do not have much influence on the results that we discuss next. After fitting the parameters for the fiducial simulation set, we consider one cosmological parameter and take two values of it at $\pm\delta p_m$ away from the fiducial value $\bar{p}_m$ and run the simulations. We choose the δp_m values such that the parameters $\{A_{\text{vel}}, c_0, c1, c2\}$ stay close to the values for the fiducial simulation. Next, we seek the best fit $a_\parallel$ value for simulations with $(\bar{p}_m \pm \delta p_m)$ at the same z_{half} as the fiducial simulations, while keeping $\{A_{\text{vel}}, c_0, c1, c2\}$ values fixed. We also use the fiducial parameter set to determine $H^{\text{fid}}(z)$ and r_d^{fid} values. This process ensures that the change δp_m will only change the $a_\parallel$ values. After getting the two $a_\parallel$ values at $(\bar{p}_m \pm \delta p_m)$, we calculate the coefficient $\frac{\partial \ln a_\parallel}{\partial p_m}(\mathbf{p})$. We apply the same process for all the cosmological parameters, and find that only Ω_{m0} and Ω_{b0} change the $a_\parallel$ values significantly, which is expected. Like in Sec. V B, we also do not consider the variation of the parameter $a_\perp$, while performing the fitting process. Note that the uncertainties Δp_m in Eq. (13) are from Planck measurement. In order to determine the relative uncertainty $(\Delta a_\parallel/a_\parallel)$ due to Δp_m, we do the following. We draw $\mathcal{O}(10^5)$ samples for the set $(\Omega_{m0}, \Omega_{b0})$ from different Planck-2018 [9] likelihoods, determine $(\Delta a_\parallel/a_\parallel)$ for each set using Eq. (13) and get a distribution of $(\Delta a_\parallel/a_\parallel)$ values. The 1-σ uncertainty in $(\Delta a_\parallel/a_\parallel)$ is then determined from the standard deviation of this distribution. Note that we have drawn the random samples until we reach a stable Gaussian distribution for $(\Delta a_\parallel/a_\parallel)$ with a fully converged standard deviation. We find that, for all the different simulations considered in Table III, the uncertainties in Ω_{m0} and Ω_{b0} from Planck-2018 introduce $\sim$0.08–0.2% relative error in

TABLE III. This shows the relative errors introduced in the measurement of $a_\parallel$ by the uncertainties in the Planck-2018 cosmological parameters [9] for our fiducial parameter set (Table I), under the different feedback scenarios. We have used two Planck-2018 datasets, namely $TT + \text{lowE}$ and $TT, TE, EE + \text{lowE} + \text{lensing} + \text{BAO}$, to calculate the relative errors as discussed in Sec. V C. We also mention the z_{half} values for each simulation.

Model	Feedback	z_{half}	$(\frac{\Delta a_\parallel}{a_\parallel})\%$ $TT + \text{lowE}$	$(\frac{\Delta a_\parallel}{a_\parallel})\%$ $TT, TE,$ $EE + \text{lowE} + \text{lensing} + \text{BAO}$
With Ly-α Heating	No	15.1	0.16	0.081
	Low	13.3	0.17	0.086
	Regular	12.7	0.17	0.084

Hr_d measurement. This is significant if we consider the relative error values for optimistic and even for moderate foregrounds in Table II. Note that the relative errors in Table III provide an error floor, which can be minimized only with more precise measurements of the cosmological parameters, which is possible with the next generation of experiments, like *CMB stage-4* [119], *EUCLID* galaxy survey [120], etc.

VI. SUMMARY AND CONCLUSIONS

The fluctuations in the DM-baryon relative velocity field are believed to be imprinted as well predicted acoustic oscillations called VAOs in the 21-cm power spectrum at cosmic dawn and also possibly at early reionization. These VAOs can be treated as a standard ruler to measure the expansion rate $H(z)$ at high redshifts. In this paper, we have simulated the 21-cm signal that includes the DM-baryon relative velocity fluctuation effects. We also model the VAOs in the 21-cm power spectrum using analytical prescriptions. We perform Alcock-Paczyński (AP) tests on the simulated data, and quantify the relative error with which the combination $H(z)r_d$ (or $a_\parallel$ parameter) can be measured under the different heating, LW feedback and foreground scenarios. We consider the 21-cm observations with the HERA interferometer and assume three foreground removal scenarios: optimistic, moderate and pessimistic. We contained our analysis only to EoH, which occurs at $z < z_{\text{min}}$ (where z_{min} refers to the redshift where the global signal $\langle T_{21} \rangle = \langle T_{21} \rangle_{\text{min}}$ has its minimum value), and measure $H(z)r_d$ at $z = z_{\text{half}}$ where $\langle T_{21} \rangle = (1/2)\langle T_{21} \rangle_{\text{min}}$ and the signal-to-noise for VAO measurement is highest close to this redshift. The z_{half} values change with changes in heating and LW feedback scenarios, and the change Δz_{half} can be as large as $\sim$3 between the different scenarios. We quote our main results (for the fiducial set of parameters given in Table I) in Table II. We find that, if no LW feedback is present, $H(z)r_d$ can be measured with 0.3,0.62 and 1.82% relative accuracy for optimistic, moderate and pessimistic foreground removal scenarios respectively. LW feedback tend to erase the VAO peaks and, as a result, the relative accuracy in $H(z)r_d$ measurement decreases. When we consider Lyman-α

heating in our simulations, which reduces the 21-cm power spectrum amplitude and thereby VAO peaks, we find that the errors are $\sim$1.5 times worst when compared against the simulations with no Lyman-α heating. This is a significant effect, depending on the strength of the x-ray heating.

To quantify the best possible measurement of Hr_d for all the different astrophysical and cosmological scenarios, we run 108 different simulations by changing the model parameters around the fiducial set which change the z_{min} and $\langle T_{21} \rangle_{\text{min}}$ values. We find that for $14 < z_{\text{min}} < 22$ (or $11 < z_{\text{half}} < 16$), it is possible to measure $H(z)r_d$ with $\lesssim$1.5%, $\lesssim$3% and $\lesssim$6% accuracy for optimistic, moderate and pessimistic foregrounds respectively. These results are in agreement with Ref. [64]. At $z_{\text{min}} > 22$, errors increase substantially. We checked the errors introduced by the uncertainty in cosmological parameters from Planck satellite measurements, and found that the uncertainties in Ω_{m0} and Ω_{b0} introduce $\sim$0.08–0.2% relative error in $H(z)r_d$ measurement. Considering the errors for optimistic and even for moderate foregrounds, this is significant.

Considering the local measurements, like SHOES [12], and the galaxy surveys, like Baryon Oscillation Spectroscopic Survey (BOSS) [121], we have measurement of $H(z)$ up to $z \lesssim 2$. Future galaxy surveys, like *Euclid* [122,123] and *SPHEREX* [124], are expected to measure $H(z)$ up to a maximum redshift of $z \sim 5$. Line intensity mapping (LIM) using the post reionization 21-cm signal, we can reach up to $z \sim 6$ [42,43,47,125–127]. LIM technique using other lines, like: carbon monoxide (CO) rotational lines [128–132], [CII] [133–135], $H\alpha$ and $H\beta$ [136], oxygen lines [137], Lyman-α [138], etc., can measure $H(z)$ up to $z \lesssim 9$ [49,104]. Our current work predicts that, using VAOs in the 21-cm power spectrum, it is possible to measure $H(z)$ with reasonable accuracy in the range $10 < z < 20$. The redshift range can be extended further if we include the VAOs from LCE ($z > 20$). However, we have analyzed the VAO signal from LCE and found that the current generation of 21-cm experiments, like HERA, are not very sensitive to the measurement of $H(z)$ from this epoch.

Our analysis has a few limitations which we discuss below. As the current generation 21-cm observations will mostly measure the modes with $k_\parallel \gg k_\perp$ due to the shape

of the foreground wedge, we vary $a_\parallel$ in our analysis while we keep $a_\perp$ fixed throughout. However, it is also possible to include the variation of $a_\perp$ in the analysis (as described in Ref. [64]), and this will provide a constraint on the measurement of $D_A(z)$. We have performed a separate analysis with both $a_\parallel$ and $a_\perp$ parameters for a few simulations mentioned in Table II and we got similar results as found by Ref. [64]. The constraints on $D_A(z)$ are not very good except for the optimistic foreground case. We note that the relative errors for $H(z)r_d$ in Table II are largely unaffected by the inclusion of $a_\perp$. The VAO amplitude is also affected by the additional feedback effects like: galactic winds emanating from star-forming regions [139], photo evaporation of small galaxies [140], ultraviolet radiative feedback [141], etc., which hinder the star formation in different haloes, and we do not include these in our analysis. Presence of exotic dark matters, like *warm* [142–144] and *fuzzy* [76,145,146], also affect the formation of mini haloes and thereby affect the VAO signature in the 21-cm power spectrum. Spectrum of the early x-ray sources also determine the detectability of VAOs [147,148]. Recently, Ref. [107] has pointed out that the parametrization for star formation rate density used in 21cmvFAST code does not reproduce the stellar-to-halo mass relation observed in UV luminosity functions from HST. Further, 21cmvFAST assumes isotropic LW feedback which may overpredict VAOs (see Ref. [107]). Our analysis is done for coeval boxes. VAO amplitude changes if the power spectra are calculated for light-cone boxes [107], which are more realistic. We leave all these for future study.

We finally conclude that the detection of the VAO features in the 21-cm signal using HERA radio telescope enables us to measure the expansion rate $H(z)$ of the universe during the cosmic dawn and early reionization era ($11 < z < 20$) with reasonable accuracy. The precision with which $H(z)$ can be measured is comparable to those of the low redshift measurements. This can be helpful in testing various cosmological scenarios, and also can be helpful in alleviating the ongoing "Hubble tension."

ACKNOWLEDGMENTS

[1] E. Hubble, Proc. Natl. Acad. Sci. U.S.A. **15**, 168 (1929).
[2] A. G. Riess *et al.* (Supernova Search Team Collaboration), Astron. J. **116**, 1009 (1998).
[3] S. Perlmutter *et al.* (Supernova Cosmology Project Collaboration), Astrophys. J. **517**, 565 (1999).
[4] S. Weinberg, Rev. Mod. Phys. **61**, 1 (1989).
[5] R. R. Caldwell and M. Kamionkowski, Annu. Rev. Nucl. Part. Sci. **59**, 397 (2009).
[6] A. Joyce, L. Lombriser, and F. Schmidt, Annu. Rev. Nucl. Part. Sci. **66**, 95 (2016).
[7] D. Huterer and D. L. Shafer, Rep. Prog. Phys. **81**, 016901 (2018).
[8] S. M. Carroll, Living Rev. Relativity **4**, 1 (2001).
[9] N. Aghanim *et al.* (Planck Collaboration), Astron. Astrophys. **641**, A6 (2020); **652**, C4(E) (2021).
[10] A. G. Riess, S. Casertano, W. Yuan, J. B. Bowers, L. Macri, J. C. Zinn, and D. Scolnic, Astrophys. J. Lett. **908**, L6 (2021).
[11] K. C. Wong, S. H. Suyu, G. C. F. Chen, C. E. Rusu, M. Millon, D. Sluse, V. Bonvin, C. D. Fassnacht, S. Taubenberger, M. W. Auger *et al.*, Mon. Not. R. Astron. Soc. **498**, 1420 (2020).
[12] E. Di Valentino, L. A. Anchordoqui, O. Akarsu, Y. Ali-Haimoud, L. Amendola, N. Arendse, M. Asgari, M. Ballardini, S. Basilakos, and E. Battistelli *et al.*, Astropart. Phys. **131**, 102605 (2021).
[13] L. Knox and M. Millea, Phys. Rev. D **101**, 043533 (2020).
[14] K. Jedamzik, L. Pogosian, and G. B. Zhao, Commun. Phys. **4**, 123 (2021).
[15] J. C. Hill, E. McDonough, M. W. Toomey, and S. Alexander, Phys. Rev. D **102**, 043507 (2020).
[16] M. M. Ivanov, E. McDonough, J. C. Hill, M. Simonović, M. W. Toomey, S. Alexander, and M. Zaldarriaga, Phys. Rev. D **102**, 103502 (2020).
[17] G. D'Amico, L. Senatore, and P. Zhang, J. Cosmol. Astropart. Phys. 01 (2021) 006.
[18] T. L. Smith, V. Poulin, J. L. Bernal, K. K. Boddy, M. Kamionkowski, and R. Murgia, Phys. Rev. D **103**, 123542 (2021).
[19] V. Poulin, T. L. Smith, D. Grin, T. Karwal, and M. Kamionkowski, Phys. Rev. D **98**, 083525 (2018).
[20] T. L. Smith, V. Poulin, and M. A. Amin, Phys. Rev. D **101**, 063523 (2020).
[21] P. Agrawal, F. Y. Cyr-Racine, D. Pinner, and L. Randall, arXiv:1904.01016.
[22] S. Alexander and E. McDonough, Phys. Lett. B **797**, 134830 (2019).
[23] M. X. Lin, G. Benevento, W. Hu, and M. Raveri, Phys. Rev. D **100**, 063542 (2019).
[24] J. Sakstein and M. Trodden, Phys. Rev. Lett. **124**, 161301 (2020).
[25] F. Niedermann and M. S. Sloth, Phys. Rev. D **102**, 063527 (2020).
[26] N. Kaloper, Int. J. Mod. Phys. D **28**, 1944017 (2019).

[27] K. V. Berghaus and T. Karwal, Phys. Rev. D **101,** 083537 (2020).

[28] T. Adi and E. D. Kovetz, Phys. Rev. D **103,** 023530 (2021).

[29] S. Banerjee, M. Petronikolou, and E. N. Saridakis, arXiv:2209.02426.

[30] M. Petronikolou, S. Basilakos, and E. N. Saridakis, Phys. Rev. D **106,** 124051 (2022).

[31] E. Di Valentino, O. Mena, S. Pan, L. Visinelli, W. Yang, A. Melchiorri, D. F. Mota, A. G. Riess, and J. Silk, Classical Quantum Gravity **38,** 153001 (2021).

[32] M. G. Dainotti, B. De Simone, T. Schiavone, G. Montani, E. Rinaldi, and G. Lambiase, Astrophys. J. **912,** 150 (2021).

[33] M. G. Dainotti, B. De Simone, T. Schiavone, G. Montani, E. Rinaldi, G. Lambiase, M. Bogdan, and S. Ugale, Galaxies **10,** 24 (2022).

[34] M. Dixon et al. (DES Collaboration), Mon. Not. R. Astron. Soc. **517,** 4291 (2022).

[35] P. Madau, A. Meiksin, and M. J. Rees, Astrophys. J. **475,** 429 (1997).

[36] R. Barkana and A. Loeb, Phys. Rep. **349,** 125 (2001).

[37] S. Bharadwaj, B. B. Nath, B. B. Nath, and S. K. Sethi, J. Astrophys. Astron. **22,** 21 (2001).

[38] S. Furlanetto, S. P. Oh, and F. Briggs, Phys. Rep. **433,** 181 (2006).

[39] S. Wyithe and A. Loeb, Mon. Not. R. Astron. Soc. **383,** 606 (2008).

[40] A. Lewis and A. Challinor, Phys. Rev. D **76,** 083005 (2007).

[41] J. R. Pritchard and A. Loeb, Phys. Rev. D **78,** 103511 (2008).

[42] D. Sarkar, S. Bharadwaj, and S. Anathpindika, Mon. Not. R. Astron. Soc. **460,** 4310 (2016).

[43] D. Sarkar and S. Bharadwaj, Mon. Not. R. Astron. Soc. **476,** 96 (2018).

[44] D. Sarkar and S. Bharadwaj, Mon. Not. R. Astron. Soc. **487,** 5666 (2019).

[45] D. Sarkar, S. Majumdar, and S. Bharadwaj, Mon. Not. R. Astron. Soc. **490,** 2880 (2019).

[46] S. Bharadwaj, S. K. Sethi, and T. D. Saini, Phys. Rev. D **79,** 083538 (2009).

[47] A. Obuljen, E. Castorina, F. Villaescusa-Navarro, and M. Viel, J. Cosmol. Astropart. Phys. 05 (2018) 004.

[48] S. Camera and H. Padmanabhan, Mon. Not. R. Astron. Soc. **496,** 4115 (2020).

[49] J. L. Bernal, P. C. Breysse, H. Gil-Marín, and E. D. Kovetz, Phys. Rev. D **100,** 123522 (2019).

[50] B. Ciardi, E. Scannapieco, F. Stoehr, A. Ferrara, I. T. Iliev, and P. R. Shapiro, Mon. Not. R. Astron. Soc. **366,** 689 (2006).

[51] T. Kimm, H. Katz, M. Haehnelt, J. Rosdahl, J. Devriendt, and A. Slyz, Mon. Not. R. Astron. Soc. **466,** 4826 (2017).

[52] Y. Qin, A. Mesinger, J. Park, B. Greig, and J. B. Muñoz, Mon. Not. R. Astron. Soc. **495,** 123 (2020).

[53] E. Bertschinger, Annu. Rev. Astron. Astrophys. **36,** 599 (1998).

[54] R. S. Somerville and R. Davé, Annu. Rev. Astron. Astrophys. **53,** 51 (2015).

[55] L. E. Strigari, M. Kaplinghat, and J. S. Bullock, Phys. Rev. D **75,** 061303 (2007).

[56] A. Fialkov, Int. J. Mod. Phys. D **23,** 1430017 (2014).

[57] R. Barkana, Phys. Rep. **645,** 1 (2016).

[58] D. Tseliakhovich and C. Hirata, Phys. Rev. D **82,** 083520 (2010).

[59] J. Bovy and C. Dvorkin, Astrophys. J. **768,** 70 (2013).

[60] A. Stacy, V. Bromm, and A. Loeb, Astrophys. J. Lett. **730,** L1 (2011).

[61] A. Fialkov, R. Barkana, D. Tseliakhovich, and C. M. Hirata, Mon. Not. R. Astron. Soc. **424,** 1335 (2012).

[62] F. Schmidt, Phys. Rev. D **94,** 063508 (2016).

[63] J. B. Muñoz, Phys. Rev. D **100,** 063538 (2019).

[64] J. B. Muñoz, Phys. Rev. Lett. **123,** 131301 (2019).

[65] D. R. DeBoer, A. R. Parsons, J. E. Aguirre, P. Alexander, Z. S. Ali, A. P. Beardsley, G. Bernardi, J. D. Bowman, R. F. Bradley, and C. L. Carilli et al., Publ. Astron. Soc. Pac. **129,** 045001 (2017).

[66] Z. Haiman, M. J. Rees, and A. Loeb, Astrophys. J. **476,** 458 (1997).

[67] M. Ricotti, N. Y. Gnedin, and J. M. Shull, Astrophys. J. **560,** 580 (2001).

[68] E. Visbal, Z. Haiman, B. Terrazas, G. L. Bryan, and R. Barkana, Mon. Not. R. Astron. Soc. **445,** 107 (2014).

[69] L. Chuzhoy and P. R. Shapiro, Astrophys. J. **655,** 843 (2007).

[70] X. L. Chen and J. Miralda-Escude, Astrophys. J. **602,** 1 (2004).

[71] A. Oklopčić and C. M. Hirata, Astrophys. J. **779,** 146 (2013).

[72] B. Ciardi, R. Salvaterra, and T. Di Matteo, Mon. Not. R. Astron. Soc. **401,** 2635 (2010).

[73] S. Mittal and G. Kulkarni, Mon. Not. R. Astron. Soc. **503,** 4264 (2021).

[74] T. Venumadhav, L. Dai, A. Kaurov, and M. Zaldarriaga, Phys. Rev. D **98,** 103513 (2018).

[75] A. Meiksin, Res. Notes AAS **5,** 126 (2021).

[76] D. Sarkar, J. Flitter, and E. D. Kovetz, Phys. Rev. D **105,** 103529 (2022).

[77] S. A. Wouthuysen, Astron. J. **57,** 31 (1952).

[78] George B. Field, Proc. Ire. **46,** 240 (1958).

[79] C. M. Hirata, Mon. Not. R. Astron. Soc. **367,** 259 (2006).

[80] S. Furlanetto and M. Furlanetto, Mon. Not. R. Astron. Soc. **374,** 547 (2007).

[81] P. R. Shapiro, K. Ahn, M. A. Alvarez, I. T. Iliev, H. Martel, and D. Ryu, Astrophys. J. **646,** 681 (2006).

[82] G. Mellema, L. V. E. Koopmans, F. A. Abdalla, G. Bernardi, B. Ciardi, S. Daiboo, A. G. de Bruyn, K. K. Datta, H. Falcke, and A. Ferrara et al., Exp. Astron. **36,** 235 (2013).

[83] P. Ocvirk, N. Gillet, P. R. Shapiro, D. Aubert, I. T. Iliev, R. Teyssier, G. Yepes, J. H. Choi, D. Sullivan, and A. Knebe et al., Mon. Not. R. Astron. Soc. **463,** 1462 (2016).

[84] J. Park, A. Mesinger, B. Greig, and N. Gillet, Mon. Not. R. Astron. Soc. **484,** 933 (2019).

[85] H. Xu, K. Ahn, J. H. Wise, M. L. Norman, and B. W. O'Shea, Astrophys. J. **791,** 110 (2014).

[86] A. Ewall-Wice, J. Hewitt, A. Mesinger, J. S. Dillon, A. Liu, and J. Pober, Mon. Not. R. Astron. Soc. **458,** 2710 (2016).

[87] S. Sazonov and I. Khabibullin, Astron. Lett. **43,** 211 (2017).

[88] A. J. Benson, N. Sugiyama, A. Nusser, and C. G. Lacey, Mon. Not. R. Astron. Soc. **369,** 1055 (2006).

[89] A. Fialkov, R. Barkana, A. Pinhas, and E. Visbal, Mon. Not. R. Astron. Soc. **437,** L36 (2014).

[90] N. Dalal, U. L. Pen, and U. Seljak, J. Cosmol. Astropart. Phys. 11 (2010) 007.

[91] S. Naoz, N. Yoshida, and N. Y. Gnedin, Astrophys. J. **747,** 128 (2012).

[92] T. Greif, S. White, R. Klessen, and V. Springel, Astrophys. J. **736,** 147 (2011).

[93] M. McQuinn and R. M. O'Leary, Astrophys. J. **760,** 3 (2012).

[94] J. Yoo, N. Dalal, and U. Seljak, J. Cosmol. Astropart. Phys. 07 (2011) 018.

[95] J. R. Pritchard and A. Loeb, Rep. Prog. Phys. **75,** 086901 (2012).

[96] D. Tseliakhovich, R. Barkana, and C. Hirata, Mon. Not. R. Astron. Soc. **418,** 906 (2011).

[97] J. Lesgourgues, arXiv:1104.2932.

[98] D. Blas, J. Lesgourgues, and T. Tram, J. Cosmol. Astropart. Phys. 07 (2011) 034.

[99] J. Lesgourgues, arXiv:1104.2934.

[100] J. Lesgourgues and T. Tram, J. Cosmol. Astropart. Phys. 09 (2011) 032.

[101] C. Alcock and B. Paczynski, Nature (London) **281,** 358 (1979).

[102] R. Barkana, Mon. Not. R. Astron. Soc. **372,** 259 (2006).

[103] X. D. Li, H. Miao, X. Wang, X. Zhang, F. Fang, X. Luo, Q. G. Huang, and M. Li, Astrophys. J. **875,** 92 (2019).

[104] J. L. Bernal, P. C. Breysse, and E. D. Kovetz, Phys. Rev. Lett. **123,** 251301 (2019).

[105] F. Melia, J. Qin, and T. J. Zhang, Mon. Not. R. Astron. Soc. **499,** L36 (2020).

[106] A. Mesinger, S. Furlanetto, and R. Cen, Mon. Not. R. Astron. Soc. **411,** 955 (2011).

[107] J. B. Muñoz, Y. Qin, A. Mesinger, S. G. Murray, B. Greig, and C. Mason, Mon. Not. R. Astron. Soc. **511,** 3657 (2022).

[108] Z. Abdurashidova et al. (HERA Collaboration), Astrophys. J. **924,** 51 (2022).

[109] Z. Abdurashidova et al. (HERA Collaboration), Astrophys. J. **925,** 221 (2022).

[110] J. D. Bowman, M. F. Morales, and J. N. Hewitt, Astrophys. J. **695,** 183 (2009).

[111] J. S. Dillon, A. Liu, and M. Tegmark, Phys. Rev. D **87,** 043005 (2013).

[112] B. J. Hazelton, M. F. Morales, and I. S. Sullivan, Astrophys. J. **770,** 156 (2013).

[113] A. Liu and M. Tegmark, Phys. Rev. D **83,** 103006 (2011).

[114] A. Datta, J. D. Bowman, and C. L. Carilli, Astrophys. J. **724,** 526 (2010).

[115] J. C. Pober, A. Liu, J. S. Dillon, J. E. Aguirre, J. D. Bowman, R. F. Bradley, C. L. Carilli, D. R. DeBoer, J. N. Hewitt, D. C. Jacobs et al., Astrophys. J. **782,** 66 (2014).

[116] J. C. Pober, A. R. Parsons, D. R. DeBoer, P. McDonald, M. McQuinn, J. E. Aguirre, Z. Ali, R. F. Bradley, T. C. Chang, and M. F. Morales, Astron. J. **145,** 65 (2013).

[117] D. Foreman-Mackey, D. W. Hogg, D. Lang, and J. Goodman, Publ. Astron. Soc. Pac. **125,** 306 (2013).

[118] A. Liu, J. R. Pritchard, R. Allison, A. R. Parsons, U. Seljak, and B. D. Sherwin, Phys. Rev. D **93,** 043013 (2016).

[119] K. Abazajian et al. (CMB-S4 Collaboration), arXiv:2203.08024.

[120] L. Amendola et al. (Euclid Theory Working Group Collaboration), Living Rev. Relativity **16,** 6 (2013).

[121] M. M. Ivanov, M. Simonović, and M. Zaldarriaga, J. Cosmol. Astropart. Phys. 05 (2020) 042.

[122] S. Ilić et al. (Euclid Collaboration), Astron. Astrophys. **657,** A91 (2022).

[123] A. Mazumdar, D. Sarkar, and S. Bharadwaj, arXiv:2209.03233.

[124] O. Doré, J. Bock, P. Capak, R. de Putter, T. Eifler, C. Hirata, P. Korngut, E. Krause, D. Masters, A. Raccanelli et al., arXiv:1412.4872.

[125] A. Pourtsidou, D. Bacon, and R. Crittenden, Mon. Not. R. Astron. Soc. **470,** 4251 (2017).

[126] L. C. Olivari, C. Dickinson, R. A. Battye, Y. Z. Ma, A. A. Costa, M. Remazeilles, and S. Harper, Mon. Not. R. Astron. Soc. **473,** 4242 (2018).

[127] A. Chakraborty, A. Datta, N. Roy, S. Bharadwaj, T. R. Choudhury, K. K. Datta, S. Pal, M. Choudhury, S. Choudhuri, P. Dutta et al., Astrophys. J. Lett. **907,** L7 (2021).

[128] A. Lidz, S. R. Furlanetto, S. P. Oh, J. Aguirre, T. C. Chang, O. Dore, and J. R. Pritchard, Astrophys. J. **741,** 70 (2011).

[129] A. Pullen, T. C. Chang, O. Dore, and A. Lidz, Astrophys. J. **768,** 15 (2013).

[130] P. C. Breysse, E. D. Kovetz, and M. Kamionkowski, Mon. Not. R. Astron. Soc. **443,** 3506 (2014).

[131] H. Padmanabhan, Mon. Not. R. Astron. Soc. **475,** 1477 (2018).

[132] S. Libanore, C. Unal, D. Sarkar, and E. D. Kovetz, Phys. Rev. D **106,** 123512 (2022).

[133] M. B. Silva, M. G. Santos, A. Cooray, and Y. Gong, Astrophys. J. **806,** 209 (2015).

[134] A. R. Pullen, P. Serra, T. C. Chang, O. Dore, and S. Ho, Mon. Not. R. Astron. Soc. **478,** 1911 (2018).

[135] H. Padmanabhan, Mon. Not. R. Astron. Soc. **488,** 3014 (2019).

[136] B. M. Silva, S. Zaroubi, R. Kooistra, and A. Cooray, Mon. Not. R. Astron. Soc. **475,** 1587 (2018).

[137] Y. Gong, A. Cooray, M. B. Silva, M. Zemcov, C. Feng, M. G. Santos, O. Dore, and X. Chen, Astrophys. J. **835,** 273 (2017).

[138] A. R. Pullen, O. Dore, and J. Bock, Astrophys. J. **786,** 111 (2014).

[139] V. Springel and L. Hernquist, Mon. Not. R. Astron. Soc. **339,** 312 (2003).

[140] R. Barkana and A. Loeb, Astrophys. J. **523,** 54 (1999).

[141] A. Mesinger and M. Dijkstra, Mon. Not. R. Astron. Soc. **390,** 1071 (2008).

[142] M. Sitwell, A. Mesinger, Y. Z. Ma, and K. Sigurdson, Mon. Not. R. Astron. Soc. **438,** 2664 (2014).

[143] A. Boyarsky, D. Iakubovskyi, O. Ruchayskiy, A. Rudakovskyi, and W. Valkenburg, Phys. Rev. D **100,** 123005 (2019).

[144] J. B. Muñoz, C. Dvorkin, and F. Y. Cyr-Racine, Phys. Rev. D **101,** 063526 (2020).

[145] D. Jones, S. Palatnick, R. Chen, A. Beane, and A. Lidz, Astrophys. J. **913**, 7 (2021).

[146] S. C. Hotinli, D. J. E. Marsh, and M. Kamionkowski, Phys. Rev. D **106**, 043529 (2022).

[147] F. Pacucci, A. Mesinger, S. Mineo, and A. Ferrara, Mon. Not. R. Astron. Soc. **443**, 678 (2014).

[148] A. Fialkov, R. Barkana, and E. Visbal, Nature (London) **506**, 197 (2014).